

**High-order Fermi arcs and topological phase transitions in the kagome semimetal  $\text{Pt}_3\text{P}_2\text{Te}_8$** Pengyu Zheng,<sup>1</sup> Changtan Wan,<sup>1</sup> Zhihong Yuan,<sup>2</sup> Jingjing Meng,<sup>1</sup> Yiran Peng,<sup>1</sup> Rui Liu,<sup>1</sup> and Zhiping Yin<sup>1,3,\*</sup><sup>1</sup>*Department of Physics and Center for Advanced Quantum Studies, Beijing Normal University, Beijing 100875, China*<sup>2</sup>*School of Physics and Information Engineering, Shanxi Normal University, Taiyuan 030031, China*<sup>3</sup>*Key Laboratory of Multiscale Spin Physics (Ministry of Education), Beijing Normal University, Beijing 100875, China*

(Received 6 October 2023; accepted 22 January 2024; published 1 February 2024)

We design a kagome compound  $\text{Pt}_3\text{P}_2\text{Te}_8$  and find it is a topological semimetal with a symmetry-protected three-dimensional (3D) bulk Dirac point along the  $\Gamma$ -A path. This Dirac point is not intrinsic to kagome lattice and brings a parity inversion, leading to topological surface states and fragile Fermi arcs on the (100) surface. These features are very close to the Fermi level and distinct from the bulk states, which suggests they can be observed in experiments. We further characterize the 3D bulk Dirac point and compute a high-order topological invariant, i.e., the change of the filling anomaly, whose value of 4 indicates the high-order bulk-hinge correspondence and the existence of high-order Fermi arcs. Moreover,  $\text{Pt}_3\text{P}_2\text{Te}_8$  exhibits rich topological phase transitions under hydrostatic pressure. Our results provide a potential platform to study topological properties related to 3D bulk Dirac points and pressure-induced topological phase transitions in the kagome lattice.

DOI: [10.1103/PhysRevB.109.085102](https://doi.org/10.1103/PhysRevB.109.085102)**I. INTRODUCTION**

Kagome lattices, due to their rich intrinsic properties such as flat bands, Dirac points, and saddle points, have attracted lots of interest [1–11]. Flat band, which comes from the destructive interference of electronic wave functions in the kagome lattice, is known to favor ferromagnetism, high-temperature superconductivity, and fractional quantum Hall effects [12–15]. In contrast to flat band with vanishing velocity, high-velocity (massive) Dirac/Weyl fermions accompanied with large intrinsic anomalous Hall effects in kagome magnets have been reported [16–21]. Besides, saddle point can lead to various kinds of instability such as spin density wave, charge density wave, and nematicity order [22–27]. These exotic features make the kagome lattice an important platform for studying topological states and correlated many-body physics and it is meaningful to find and investigate more kagome compounds to enrich and improve this field.

In 2020, a new kagome van der Waals (vdW) semiconductor  $\text{Pd}_3\text{P}_2\text{S}_8$  was reported in which the kagome lattice is formed by Pd atoms and the Pd-P-S blocking layers are connected by interlayer vdW interaction [28]. One important feature of  $\text{Pd}_3\text{P}_2\text{S}_8$  is that it can serve as an ideal system to explore flat-band physics of two-dimensional kagome lattices because of the easy exfoliation and the presence of an extremely flat band near the Fermi level ( $E_F$ ) [28,29]. More interestingly, under high pressure,  $\text{Pd}_3\text{P}_2\text{S}_8$  exhibits metallicity at high temperatures and superconductivity emerges at low temperatures [30–32]. With Se doping, the band gap of  $\text{Pd}_3\text{P}_2(\text{S}_{1-x}\text{Se}_x)_8$  becomes smaller and the superconducting transition temperature becomes higher under the same pressure due to the enhanced intralayer and interlayer hoppings [29,30]. However, bulk  $\text{Pd}_3\text{P}_2(\text{S}_{1-x}\text{Se}_x)_8$  at ambient

pressure is still a semiconductor with a large band gap [29], which indicates it is not a topological metal like a Dirac semimetal [33] or topological insulator, which has odd band inversions around  $E_F$  [34,35].

In this work, based on the kagome semiconductors  $\text{Pd}_3\text{P}_2(\text{S}, \text{Se})_8$ , we propose a kagome compound  $\text{Pt}_3\text{P}_2\text{Te}_8$  and systematically study its electronic structure and topological property. Different from  $\text{Pd}_3\text{P}_2(\text{S}, \text{Se})_8$ , the aforementioned flat band around  $E_F$  is destroyed and  $\text{Pt}_3\text{P}_2\text{Te}_8$  becomes a semimetal, due to the more extended Te  $5p$  orbitals and the large hybridization between Te  $5p$  orbitals and Pt  $5d$  orbitals. Although the imperfect destructive quantum interference breaks the intrinsic flat band of kagome lattice, we find that  $\text{Pt}_3\text{P}_2\text{Te}_8$  is a topological semimetal with a single parity inversion and three-dimensional (3D) bulk Dirac points, which are not intrinsic to the kagome lattice. As a result, topological surface states and fragile Fermi arcs are found around  $E_F$ . We further compute a high-order topological invariant, i.e., the change of the filling anomaly to characterize the 3D bulk Dirac point. The nontrivial result indicates the higher-order bulk-hinge correspondence and the existence of high-order Fermi arcs. Finally, we investigate the influence of hydrostatic pressure and find that  $\text{Pt}_3\text{P}_2\text{Te}_8$  exhibits rich topological phase transitions. Our results suggest  $\text{Pt}_3\text{P}_2\text{Te}_8$  is a potential platform to study topological property related to 3D bulk Dirac points and pressure-induced topological phase transitions in the kagome lattice.

**II. METHODS**

We perform density functional theory (DFT) calculations to study the kagome compound  $\text{Pt}_3\text{P}_2\text{Te}_8$  by using the projector augmented wave method as implemented in Vienna *ab initio* Simulation Package (VASP) [36]. We use the Perdew-Burke-Ernzerhof (PBE) exchange correlation functional. The cutoff energy for the plane-wave basis is set to be 600 eV.

\*yinzhiping@bnu.edu.cn

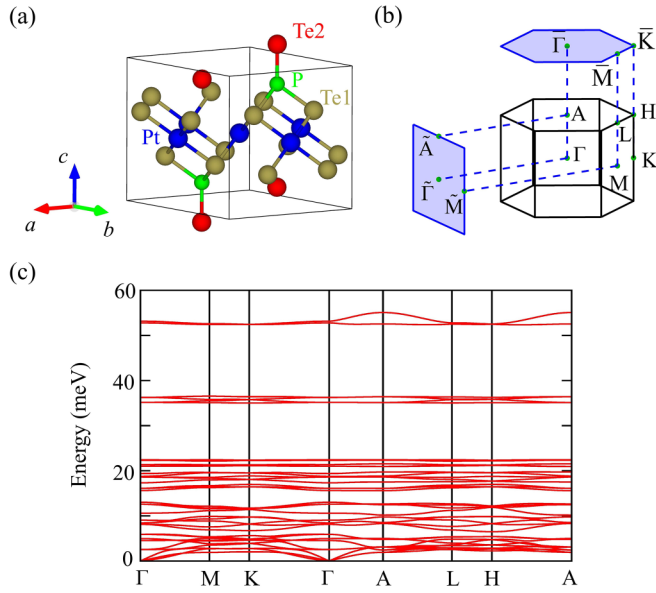


FIG. 1. The crystal structure, Brillouin zone (BZ) and phonon spectra of  $\text{Pt}_3\text{P}_2\text{Te}_8$ . (a) The crystal structure. (b) Three-dimensional BZ, projected (001) and (100) surface BZs. (c) The phonon spectrum.

The setting of the local axes of Pt follows the setting of the local axes of Pd in  $\text{Pd}_3\text{P}_2\text{S}_8$  as described in Ref. [29] and the local axes of Te are directly set to be the same as the global axes, i.e., the  $x$  axis follows the  $a$  axis and the  $z$  axis follows the  $c$  axis. The lattice parameters and internal atomic positions are optimized with the interlayer vdW interaction correction using the DFT-D3 method of Grimme [37]. The phonon spectrum is calculated by the density functional perturbation theory (DFPT) method [38] with  $2 \times 2 \times 2$  supercell. The irreducible representations of the electronic states are obtained by using IRVSP [39]. In order to calculate the surface states, we use the tight-binding (TB) method by the combination of WANNIER90 [40] and WANNIERTOOLS [41]. For the crystal structures under hydrostatic pressure, we relax the lattice parameters and internal atomic positions under the corresponding pressure. In Sec. III D, the modified Becke-Johnson (mBJ) exchange potential correction implemented in VASP [42] is taken into account to obtain accurate band structures. We also use WIEN2K [43] with PBE exchange correlation functional plus mBJ exchange potential correction for double checking, which shows good agreement with VASP calculated results.

### III. RESULTS AND DISCUSSION

#### A. Crystal structure and dynamic stability

The crystal structure and Brillouin zone (BZ) of  $\text{Pt}_3\text{P}_2\text{Te}_8$  are shown in Figs. 1(a), 1(b). Like  $\text{Pd}_3\text{P}_2\text{S}_8$  [28,29],  $\text{Pt}_3\text{P}_2\text{Te}_8$  crystallizes in the hexagonal lattice with space group  $P-3m1$  (#164) and has a layered structure in which the kagome lattice is formed by Pt atoms. The optimized lattice parameters and internal atomic positions are listed in Table I. In order to confirm the kinetic stability of  $\text{Pt}_3\text{P}_2\text{Te}_8$ , we calculate its phonon spectrum. As shown in Fig. 1(c), the absence of imaginary phonon frequency indicates  $\text{Pt}_3\text{P}_2\text{Te}_8$  is dynamically stable.

TABLE I. The optimized internal atomic positions of  $\text{Pt}_3\text{P}_2\text{Te}_8$  with lattice constants  $a = b = 7.536 \text{ \AA}$  and  $c = 8.384 \text{ \AA}$ .

| Atom | Wyckoff position | $x$   | $y$    | $z$   |
|------|------------------|-------|--------|-------|
| Pt   | 3e               | 0.5   | 0      | 0.5   |
| Te1  | 6i               | 0.171 | -0.171 | 0.679 |
| Te2  | 2d               | 1/3   | 2/3    | 0.132 |
| P    | 2d               | 1/3   | 2/3    | 0.854 |

#### B. Electronic structure and topological surface states

We first investigate the electronic structure of  $\text{Pt}_3\text{P}_2\text{Te}_8$ . The band structure without spin-orbit coupling (SOC) is shown in Fig. 2(a). Unlike  $\text{Pd}_3\text{P}_2(\text{S,Se})_8$  [29], due to the enhanced intralayer and interlayer hoppings, which originate from the more extended Te  $5p$  orbitals, the highest valence band and the lowest conduction band overlaps and makes  $\text{Pt}_3\text{P}_2\text{Te}_8$  become a metal. In the meantime, because the kagome lattice is formed by Pt atoms and Pt  $5d$  orbitals strongly hybridize with Te  $5p$  orbitals around  $E_F$  [Fig. 2(c)], the intrinsic flat band of kagome lattice around  $E_F$  seen in  $\text{Pd}_3\text{P}_2(\text{S,Se})_8$  [29] is destroyed in  $\text{Pt}_3\text{P}_2\text{Te}_8$  by the imperfect destructive quantum interference of the Pt  $5d$  orbitals. The calculated total density of states (DOS) is very small at  $E_F$ , exhibiting semimetallic characteristic [Fig. 2(c)]. The orbital-resolved DOS results show that the band structure around  $E_F$  is mainly contributed by Te  $5p$  and Pt  $5d$  ( $d_{r2g}$  and  $d_{z^2}$ ) orbitals [Figs. 2(c), 2(d)]. The features of kagome lattice, i.e., flat band, saddle point, Dirac point can be found in the

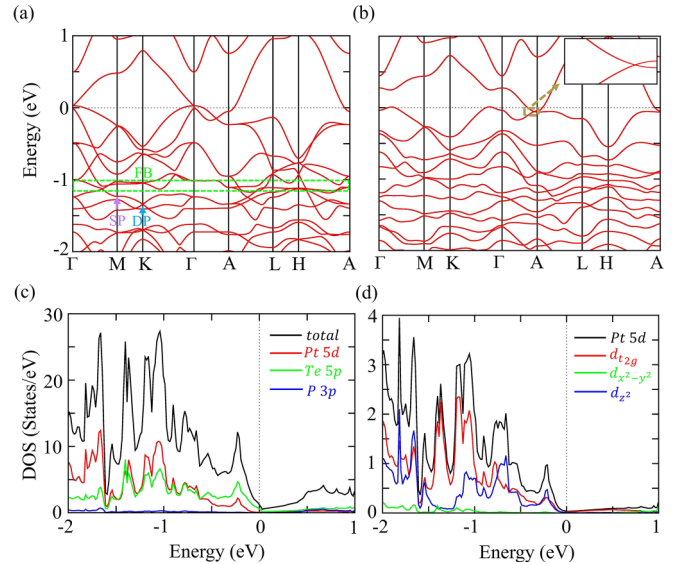
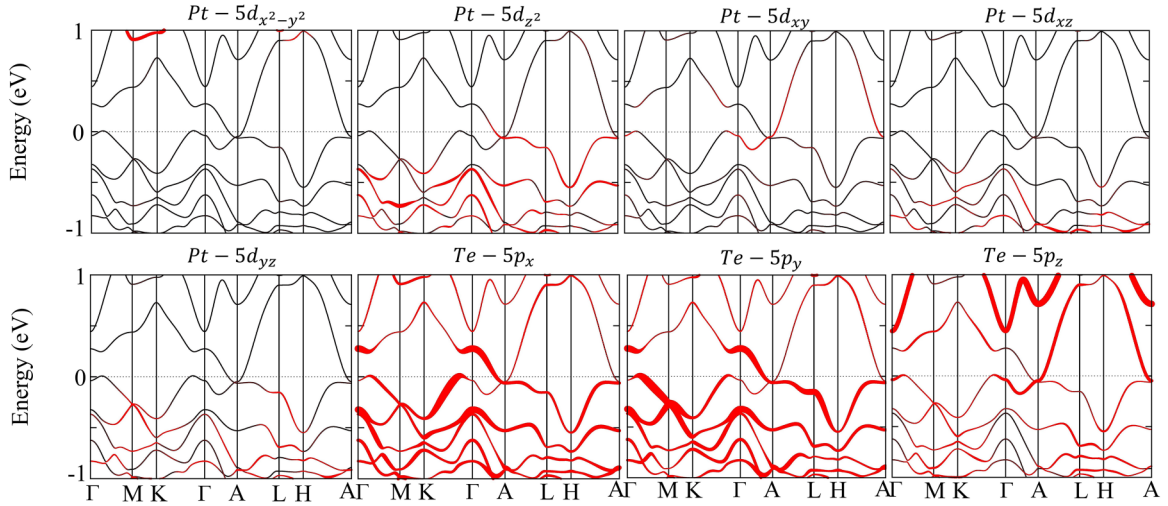


FIG. 2. The band structure and density of states (DOS) of  $\text{Pt}_3\text{P}_2\text{Te}_8$ . The band structure (a) without and (b) with spin-orbit coupling (SOC). In (a), we use the purple arrow, cyan arrow, and green dashed box to mark the intrinsic features of kagome lattice, i.e., the saddle point (SP) at  $M$  point, Dirac point (DP) at  $K$  point, and flat band (FB), respectively. In (b), we use the brown dashed box to mark the Dirac point along  $\Gamma$ -A near  $E_F$  and the inset shows the zoom-in result. (c), (d) The total and orbital-resolved partial DOS without SOC.

FIG. 3. The fat bands of  $\text{Pt}_3\text{P}_2\text{Te}_8$  with SOC.

band structure of  $\text{Pt}_3\text{P}_2\text{Te}_8$ , which are marked in Fig. 2(a) but they are not close to  $E_F$  because the contribution of Pt  $5d$  orbitals is prominent below  $-1$  eV [Fig. 2(c)]. After considering SOC, due to the large SOC strength of Pt and Te, there are significant changes in the band structure [Fig. 2(b)]. Most importantly, we find a Dirac point that is not intrinsic to kagome lattice along  $\Gamma$ -A marked by the brown dashed box in Fig. 2(b), which is vital for the nontrivial topological property of  $\text{Pt}_3\text{P}_2\text{Te}_8$  as discussed below.

As can be seen in Fig. 4(a), the band crossing of interest occurs between two bands with different irreducible representations  $\text{DT}_4 + \text{DT}_5$  (mainly composed of Te  $5p_x + p_y$  and Pt  $5d_{z^2}$  orbitals) and  $\text{DT}_6$  (mainly composed of Pt  $5d_{xy}$  and Te  $5p_z$  orbitals) (Fig. 3), which means the crossing is protected by the  $C_{3v}$  symmetry and the crossing point is a Dirac point. Besides, we also check the parities of the electronic states and parity inversion. Based on the Fu-Kane criterion on the  $Z_2$  invariant of materials with inversion symmetry [34], we

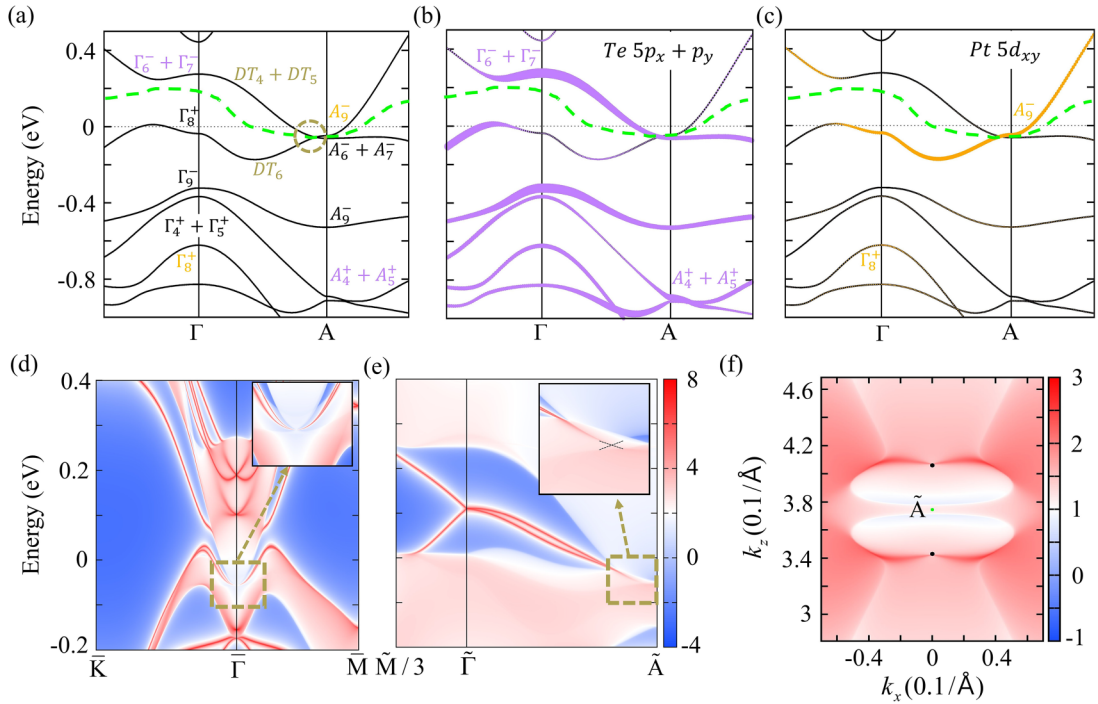


FIG. 4. The irreducible representations, fat bands, surface states, and constant-energy surface of  $\text{Pt}_3\text{P}_2\text{Te}_8$ . (a) The irreducible representations along  $\Gamma$ -A around  $E_F$ . The Dirac point is marked by the brown dashed circle. (b), (c) The fatbands of Te  $5p_x + p_y$  (b) and Pt  $5d_{xy}$  (c) orbitals. In (a)–(c), the green dashed lines represent the Fermi curves. (d), (e) The surface spectral function on the (001) and (100) surfaces (Fig. S1) [44], respectively, where the projections of the bulk Dirac points are marked by the brown dashed boxes while the insets show the zoom-in results. In the inset of (e), the black dashed lines are used for the guidelines of the projection of the bulk Dirac point. (f) The constant-energy surface on the (100) surface at  $E = E_{\text{DP}}$ . The black and green solid dots represent the projection of the bulk Dirac points and  $\tilde{A}$  in the (100) surface BZ, respectively.

TABLE II. The number of the even and odd parity states at all time-reversal-invariant momenta below the Fermi curve defined in Fig. 3(a) by the green dashed line.

| parity | $\Gamma$ | $M$ | $A$ | $L$ |
|--------|----------|-----|-----|-----|
| even   | 24       | 15  | 11  | 19  |
| odd    | 10       | 19  | 23  | 15  |

need to know the parity product of all the electronic states at eight time-reversal-invariant momenta (TRIM) below  $E_F$  for insulators or a Fermi curve for (semi)metals whose  $E_F$  is momentum dependent [45,46]. There are three equivalent TRIM  $M$  points and  $L$  points, one  $\Gamma$  point and  $A$  point in the BZ of  $\text{Pt}_3\text{P}_2\text{Te}_8$ . Hence, we need these four TRIM ( $\Gamma$ ,  $A$ ,  $M$ , and  $L$ ) to determine the  $Z_2$  invariant. We show the parity results in Table II based on the Fermi curve plotted in Fig. 4(a), which can be well defined once the  $C_{3v}$  symmetry is broken by some perturbations such as a slight increase of  $a$ , making  $a \neq b$ . We obtain the  $Z_2$  invariant (1;000). The reason of the nontrivial  $Z_2$  topological invariant is the parity inversion happened between  $\Gamma_6^- + \Gamma_7^-$  ( $A_4^+ + A_5^+$ ) and  $\Gamma_8^+$  ( $A_9^-$ ) along  $\Gamma$ - $A$ , and they can be attributed by the contribution of Te  $5p_x + p_y$  and Pt  $5d_{xy}$  orbitals (the contribution of Pt  $5d_{xy}$  orbitals for the  $\Gamma_8^+$  state is larger than that of Te  $5p_z$  orbitals), respectively [Figs. 4(b), 4(c)].

This unique electronic structure of  $\text{Pt}_3\text{P}_2\text{Te}_8$ , namely, the coexistence of the Dirac point and a single parity inversion, is similar to the cases of  $\text{Na}_3\text{Bi}$  [47] and  $\beta$ - $\text{CuI}$  [48]. We show the calculated (001) surface spectral function in Fig. 4(d). The projections of the bulk Dirac points and topological surface states can be clearly seen around  $E_F$ , which are different from the case of topological insulator (TI) [49]. We also plot the (100) surface spectral function in Fig. 4(e). In addition to the projection of the bulk Dirac point and the corresponding topological surface states, which connect the projection of the bulk Dirac point and the surface Dirac point along  $\tilde{\Gamma}$ - $\tilde{A}$ , we can also see the TI-like topological surface states along  $\tilde{\Gamma}$ - $\tilde{M}/3$  in Fig. 4(e).

A Dirac point can be viewed as the superposition of two Weyl points, which means there are double Fermi arcs originating from it. It is interesting to know how the Fermi arcs are connected. We plot the constant-energy surface at the energy of the bulk Dirac point ( $E_{\text{DP}} = E_F - 55$  meV) in Fig. 4(f). The double Fermi arc feature can be seen around the projection of the bulk Dirac point. We further plot them at different energy around  $E_{\text{DP}}$  to see their evolution with energy. As can be seen in Fig. 5, the double Fermi arcs feature can be clearly seen at  $E_{\text{DP}}$  but once the energy deviates from  $E_{\text{DP}}$ , the Fermi arcs no longer connect the projections of the bulk Dirac points but deform into Fermi contours, which indicates the fragile nature of Fermi arcs of Dirac semimetals [48,50–54].

### C. High-order topological invariant for the bulk Dirac point

Unlike Weyl semimetals, the Fermi arcs of Dirac semimetals are not truly the consequence of bulk-edge correspondence because unlike Weyl points, the Dirac points are not a source of Berry curvature [48,53,54]. In this situation, a higher-order bulk-hinge correspondence has been proposed that the

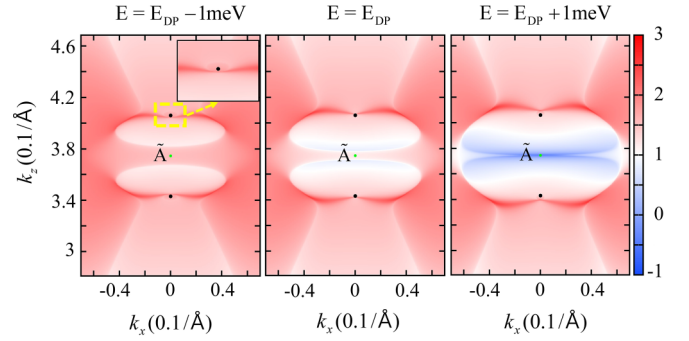


FIG. 5. The constant-energy surface on the (100) surface at different energies in which the projections of the bulk Dirac points and  $\tilde{A}$  in the (001) surface BZ are marked by the black and green solid dots, respectively. The inset of  $E = E_{\text{DP}} - 1$  meV shows the zoom-in result around the projection of the bulk Dirac points.

topologically nontrivial 3D bulk Dirac point directly results in one-dimensional high-order Fermi arcs [55–58]. One important high-order topological invariant  $\Delta\eta$ , i.e., the change of the filling anomaly [58–60] can be used to characterize the 3D bulk Dirac point. It is interesting to calculate this topological invariant for  $\text{Pt}_3\text{P}_2\text{Te}_8$  to verify whether it is a new candidate, which can host high-order Fermi arcs.

With the help of symmetry indicator [59], we can calculate  $\Delta\eta$  using the following formula in our case

$$\Delta\eta = (-2[K_{1/2}] - 2[K'_{1/2}]) - (-2[H_{1/2}] - 2[H'_{1/2}]) \bmod 6 \quad (1)$$

in which  $[K_{1/2}] = \#K_{1/2} - \#\Gamma_{1/2}$ ,  $[K'_{1/2}] = \#K'_{1/2} - \#\Gamma_{1/2}$ ,  $[H_{1/2}] = \#H_{1/2} - \#A_{1/2}$ ,  $[H'_{1/2}] = \#H'_{1/2} - \#A_{1/2}$ , and  $\#P_\rho$  represents the number of the irreducible representation  $\rho$  at the high-symmetry point  $P$  in the occupied bands (below the defined Fermi curve) and  $K(H)$  and  $K'(H')$  are equivalent in our case. We show the irreducible representations results in Table III. The difference between the occupied number of the irreducible representations with  $j_z = 1/2$  at  $\Gamma$  and  $A$  points, which originates from the symmetry-protected 3D bulk Dirac point results in a nontrivial topological invariant  $\Delta\eta = 4$ . This nontrivial high-order topological invariant indicates the higher-order bulk-hinge correspondence and the existence of high-order Fermi arcs [58,59].

### D. Topological phase transition upon hydrostatic pressure

Due to the band-gap underestimation problem in the conventional DFT-local density approximation (LDA)/PBE calculations, we use the mBJ exchange potential correction to obtain more accurate band structures. As shown in

TABLE III. The number of the irreducible representations with  $j_z = 3/2$  and  $j_z = 1/2$  at  $\Gamma$ ,  $A$ ,  $K$ , and  $H$  below the Fermi curve defined in Fig. 3(a).

|             | $\Gamma$ | $A$ | $K$ | $H$ |
|-------------|----------|-----|-----|-----|
| $j_z = 1/2$ | 23       | 22  | 23  | 23  |
| $j_z = 3/2$ | 11       | 12  | 11  | 11  |

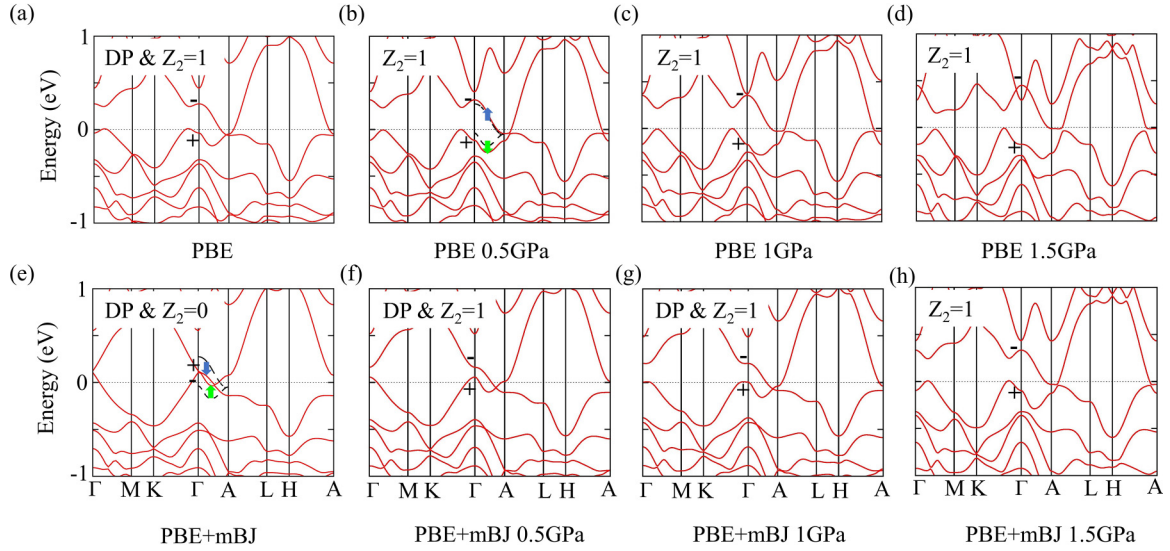


FIG. 6. The DFT-PBE and DFT-PBE+mBJ calculated band structures with SOC for the original structure and the structures with hydrostatic pressures. In (a), (e), (f), (g), although there are Dirac points, which prevent us from defining the Fermi curves, for simplicity and uniformity, we still use  $Z_2$  to label whether the single parity inversion exists or not. (a)–(d) The DFT-PBE and (e)–(h) the DFT-PBE+mBJ calculated band structures at ambient pressure (original structure) and with pressures of 0.5 GPa, 1.0 GPa, and 1.5 GPa, respectively. The parities of the electronic states at  $\Gamma$  point, which mainly determine the band inversion are marked. In (b), (e), the two DFT-PBE calculated bands of interest for the original structure along  $\Gamma$ -A are plotted by black dashed lines, while the shifting of the  $DT_4 + DT_5$  band and  $DT_6$  band are marked by blue and green arrows, respectively.

Figs. 6(a), 6(e) after considering mBJ correction, the band structure exhibits significant changes along  $\Gamma$ -A direction. The aforementioned  $DT_4 + DT_5$  band shifts down and the  $DT_6$  band shifts up, which are indicated by the blue and green arrows in Fig. 6(e), respectively. These changes reverse the parity inversion discussed above and create a new pair of Dirac points. We want to keep the coexistence of the Dirac points and a single parity inversion, which exhibits more interesting topological surface states, compared to just having Dirac points. Therefore, we calculate the electronic structure of  $Pt_3P_2Te_8$  under hydrostatic pressure and discuss the corresponding pressure-induced topological phase transitions.

The DFT-PBE calculated band structures of  $Pt_3P_2Te_8$  under hydrostatic pressures are shown in Figs. 6(b)–6(d) (the optimized lattice parameters and internal atomic positions under hydrostatic pressure are detailed in the Supplemental Material [44]). With external pressure, the  $DT_4 + DT_5$  band is shifted up whereas the  $DT_6$  band is pushed down, indicated by the blue and green arrows in Fig. 6(b), respectively, which shows an opposite trend compared to the results of mBJ correction. The shifting of the bands changes the band crossing from  $\Gamma$ -A to A-L path. Along A-L path, the band crossing is no longer protected by  $C_{3v}$  symmetry, resulting in a hybridization gap and disappearance of the counterpart Dirac point along  $\Gamma$ -A. These changes indicate that in the DFT-PBE calculated results, there is a topological phase transition between ambient pressure (original structure) and 0.5 GPa hydrostatic pressure, from the coexistence of the Dirac points and a single parity inversion to  $Z_2 = 1$  (once the Dirac points are lifted, the Fermi curve can be well defined and the  $Z_2$  can be calculated).

We turn to the DFT-PBE+mBJ calculated band structures under hydrostatic pressure. We find that with 0.5 GPa hydrostatic pressure, the system returns to the coexisting

phase, similar to the case of Fig. 6(a). As hydrostatic pressure further increases, the system undergoes a topological phase transition again from the coexisting phase to the  $Z_2 = 1$  phase, which happens between hydrostatic pressure of 1.0 GPa and 1.5 GPa. Therefore, the effect of mBJ correction to PBE is similar to some negative pressure, which destroys the coexisting phase of the original structure. However, combined with hydrostatic pressure, the system can return to the desired coexisting phase and exhibit rich topological phase transitions after considering mBJ correction.

#### IV. CONCLUSION

In conclusion, we design a kagome semimetal  $Pt_3P_2Te_8$  and systematically study its electronic structure and topological properties. Unlike the insulating  $Pd_3P_2(S,Se)_8$ , the more extended Te  $5p$  orbitals make  $Pt_3P_2Te_8$  a semimetal whose band structure around  $E_F$  is mainly contributed by Te  $5p$  and Pt  $5d$  orbitals. The intrinsic flat band, saddle point, and Dirac point of kagome lattice can be found in the band structure. After considering SOC, we find a symmetry-protected Dirac point very close to  $E_F$  along  $\Gamma$ -A, accompanied by a single parity inversion, which results in the nontrivial  $Z_2$  invariant (1;000) once the Fermi curve can be well defined. The coexistence of the Dirac points and a single parity inversion leads to topological surface states and fragile Fermi arcs around  $E_F$ . We also calculate the change of the filling anomaly  $\Delta\eta$ , which is a high-order topological invariant to characterize the 3D bulk Dirac point. We obtain the nontrivial topological invariant  $\Delta\eta = 4$ , indicating the higher-order bulk-hinge correspondence and the existence of high-order Fermi arcs. Furthermore, we investigate the influence of

hydrostatic pressure with the mBJ correction and the results exhibit rich topological phase transitions, i.e., from the phase with only Dirac points (ambient pressure) to the coexistence of the Dirac points and a single parity inversion (0.5 GPa and 1.0 GPa), and then to the  $Z_2 = 1$  phase (1.5 GPa). We notice that with proper high-pressure, superconductivity can be induced in  $\text{Pd}_3\text{P}_2(\text{S}_{1-x}\text{Se}_x)_8$  [30–32]. The compound  $\text{Pt}_3\text{P}_2\text{Te}_8$  we design is a metal at ambient pressure, which means that it may be superconducting under some lower pressure, making it a potential platform for studying the coexistence of superconductivity and topological surface states, as well as

pressure-induced topological phase transitions in the kagome lattice.

#### ACKNOWLEDGMENTS

We thank Ben-Chao Gong for useful advice. This work was supported by Innovation Program for Quantum Science and Technology (2021ZD0302800) and the National Natural Science Foundation of China (Grant No. 12074041). The calculations were carried out with high-performance computing cluster of Beijing Normal University in Zhuhai.

- [1] J.-X. Yin, B. Lian, and M. Z. Hasan, *Nature (London)* **612**, 647 (2022).
- [2] M. Li, Q. Wang, G. Wang, Z. Yuan, W. Song, R. Lou, Z. Liu, Y. Huang, Z. Liu, H. Lei, Z. Yin, and S. Wang, *Nat. Commun.* **12**, 3129 (2021).
- [3] Z. Liu, M. Li, Q. Wang, G. Wang, C. Wen, K. Jiang, X. Lu, S. Yan, Y. Huang, D. Shen, J.-X. Yin, Z. Wang, Z. Yin, H. Lei, and S. Wang, *Nat. Commun.* **11**, 4002 (2020).
- [4] K. Ohgushi, S. Murakami, and N. Nagaosa, *Phys. Rev. B* **62**, R6065(R) (2000).
- [5] L. Ye, M. Kang, J. Liu, F. von Cube, C. R. Wicker, T. Suzuki, C. Jozwiak, A. Bostwick, E. Rotenberg, D. C. Bell, L. Fu, R. Comin, and J. G. Checkelsky, *Nature (London)* **555**, 638 (2018).
- [6] T.-H. Han, J. S. Helton, S. Chu, D. G. Nocera, J. A. Rodriguez-Rivera, C. Broholm, and Y. S. Lee, *Nature (London)* **492**, 406 (2012).
- [7] T. Yu, R. Liu, Y. Peng, P. Zheng, G. Wang, X. Ma, Z. Yuan, and Z. Yin, *Phys. Rev. B* **106**, 205103 (2022).
- [8] A. Nag, Y. Peng, J. Li, S. Agrestini, H. C. Robarts, M. García-Fernández, A. C. Walters, Q. Wang, Q. Yin, H. Lei, Z. Yin, and K.-J. Zhou, *Nat. Commun.* **13**, 7317 (2022).
- [9] C. Mielke III, D. Das, J.-X. Yin, H. Liu, R. Gupta, Y.-X. Jiang, M. Medarde, X. Wu, H. C. Lei, J. Chang, P. Dai, Q. Si, H. Miao, R. Thomale, T. Neupert, Y. Shi, R. Khasanov, M. Z. Hasan, H. Luetkens, and Z. Guguchia, *Nature (London)* **602**, 245 (2022).
- [10] H. Chen, H. Yang, B. Hu, Z. Zhao, J. Yuan, Y. Xing, G. Qian, Z. Huang, G. Li, Y. Ye, S. Ma, S. Ni, H. Zhang, Q. Yin, C. Gong, Z. Tu, H. Lei, H. Tan, S. Zhou, C. Shen, X. Dong, B. Yan, Z. Wang, and H.-J. Gao, *Nature (London)* **599**, 222 (2021).
- [11] Y.-X. Jiang, J.-X. Yin, M. M. Denner, N. Shumiya, B. R. Ortiz, G. Xu, Z. Guguchia, J. He, M. S. Hossain, X. Liu, J. Ruff, L. Kautzsch, S. S. Zhang, G. Chang, I. Belopolski, Q. Zhang, T. A. Cochran, D. Multer, M. Litskevich, Z.-J. Cheng, X. P. Yang, Z. Wang, R. Thomale, T. Neupert, S. D. Wilson, and M. Z. Hasan, *Nat. Mater.* **20**, 1353 (2021).
- [12] M. Kang, S. Fang, L. Ye, H. C. Po, J. Denlinger, C. Jozwiak, A. Bostwick, E. Rotenberg, E. Kaxiras, J. G. Checkelsky, and R. Comin, *Nat. Commun.* **11**, 4004 (2020).
- [13] J.-X. Yin, S. S. Zhang, G. Chang, Q. Wang, S. S. Tsirkin, Z. Guguchia, B. Lian, H. Zhou, K. Jiang, I. Belopolski, N. Shumiya, D. Multer, M. Litskevich, T. A. Cochran, H. Lin, Z. Wang, T. Neupert, S. Jia, H. Lei, and M. Z. Hasan, *Nat. Phys.* **15**, 443 (2019).
- [14] Z. Liu, F. Liu, and Y.-S. Wu, *Chin. Phys. B* **23**, 077308 (2014).
- [15] Z. Lin, J.-H. Choi, Q. Zhang, W. Qin, S. Yi, P. Wang, L. Li, Y. Wang, H. Zhang, Z. Sun, L. Wei, S. Zhang, T. Guo, Q. Lu, J.-H. Cho, C. Zeng, and Z. Zhang, *Phys. Rev. Lett.* **121**, 096401 (2018).
- [16] J.-X. Yin, W. Ma, T. A. Cochran, X. Xu, S. S. Zhang, H.-J. Tien, N. Shumiya, G. Cheng, K. Jiang, B. Lian, Z. Song, G. Chang, I. Belopolski, D. Multer, M. Litskevich, Z.-J. Cheng, X. P. Yang, B. Swidler, H. Zhou, H. Lin, T. Neupert, Z. Wang, N. Yao, T.-R. Chang, S. Jia, and M. Zahid Hasan, *Nature (London)* **583**, 533 (2020).
- [17] W. Ma, X. Xu, J.-X. Yin, H. Yang, H. Zhou, Z.-J. Cheng, Y. Huang, Z. Qu, F. Wang, M. Z. Hasan, and S. Jia, *Phys. Rev. Lett.* **126**, 246602 (2021).
- [18] G. Xu, B. Lian, and S.-C. Zhang, *Phys. Rev. Lett.* **115**, 186802 (2015).
- [19] Q. Wang, Y. Xu, R. Lou, Z. Liu, M. Li, Y. Huang, D. Shen, H. Weng, S. Wang, and H. Lei, *Nat. Commun.* **9**, 3681 (2018).
- [20] E. Liu, Y. Sun, N. Kumar, L. Muechler, A. Sun, L. Jiao, S.-Y. Yang, D. Liu, A. Liang, Q. Xu, J. Kroder, V. Süß, H. Borrmann, C. Shekhar, Z. Wang, C. Xi, W. Wang, W. Schnelle, S. Wirth, Y. Chen, S. T. B. Goennenwein, and C. Felser, *Nat. Phys.* **14**, 1125 (2018).
- [21] S. Nakatsujii, N. Kiyohara, and T. Higo, *Nature (London)* **527**, 212 (2015).
- [22] T. Kato, Y. Li, K. Nakayama, Z. Wang, S. Souma, F. Matsui, M. Kitamura, K. Horiba, H. Kumigashira, T. Takahashi, Y. Yao, and T. Sato, *Phys. Rev. Lett.* **129**, 206402 (2022).
- [23] B. R. Ortiz, L. C. Gomes, J. R. Morey, M. Winiarski, M. Bordelon, J. S. Mangum, I. W. H. Oswald, J. A. Rodriguez-Rivera, J. R. Neilson, S. D. Wilson, E. Ertekin, T. M. McQueen, and E. S. Toberer, *Phys. Rev. Mater.* **3**, 094407 (2019).
- [24] M. Kang, S. Fang, J.-K. Kim, B. R. Ortiz, S. H. Ryu, J. Kim, J. Yoo, G. Sangiovanni, D. Di Sante, B.-G. Park, C. Jozwiak, A. Bostwick, E. Rotenberg, E. Kaxiras, S. D. Wilson, J.-H. Park, and R. Comin, *Nat. Phys.* **18**, 301 (2022).
- [25] Y. Hu, X. Wu, B. R. Ortiz, S. Ju, X. Han, J. Ma, N. C. Plumb, M. Radovic, R. Thomale, S. D. Wilson, A. P. Schnyder, and M. Shi, *Nat. Commun.* **13**, 2220 (2022).
- [26] S.-L. Yu and J.-X. Li, *Phys. Rev. B* **85**, 144402 (2012).
- [27] J.-X. Yin, S. S. Zhang, H. Li, K. Jiang, G. Chang, B. Zhang, B. Lian, C. Xiang, I. Belopolski, H. Zheng, T. A. Cochran, S.-Y. Xu, G. Bian, K. Liu, T.-R. Chang, H. Lin, Z.-Y. Lu, Z. Wang, S. Jia, W. Wang, and M. Z. Hasan, *Nature (London)* **562**, 91 (2018).

- [28] S. Park, S. Kang, H. Kim, K. H. Lee, P. Kim, S. Sim, N. Lee, B. Karuppannan, J. Kim, J. Kim, K. I. Sim, M. J. Coak, Y. Noda, C.-H. Park, J. H. Kim, and J.-G. Park, *Sci. Rep.* **10**, 20998 (2020).
- [29] S. Yan, B.-C. Gong, L. Wang, J. Wu, Q. Yin, X. Cao, X. Zhang, X. Liu, Z.-Y. Lu, K. Liu, and H. Lei, *Phys. Rev. B* **105**, 155115 (2022).
- [30] S. Li, S. Han, S. Yan, Y. Cui, L. Wang, S. Wang, S. Chen, H. Lei, F. Yuan, J. Zhang, and W. Yu, *Chin. Phys. Lett.* **39**, 067404 (2022).
- [31] Q. Wang, X.-L. Qiu, C. Pei, B.-C. Gong, L. Gao, Y. Zhao, W. Cao, C. Li, S. Zhu, M. Zhang, Y. Chen, K. Liu, and Y. Qi, *New J. Phys.* **25**, 043001 (2023).
- [32] Y. Zhou, X. He, S. Wang, J. Wang, X. Chen, Y. Zhou, C. An, M. Zhang, Z. Zhang, and Z. Yang, *Phys. Rev. B* **106**, 104512 (2022).
- [33] N. P. Armitage, E. J. Mele, and A. Vishwanath, *Rev. Mod. Phys.* **90**, 015001 (2018).
- [34] L. Fu and C. L. Kane, *Phys. Rev. B* **76**, 045302 (2007).
- [35] H. Zhang, C.-X. Liu, X.-L. Qi, X. Dai, Z. Fang, and S.-C. Zhang, *Nat. Phys.* **5**, 438 (2009).
- [36] G. Kresse and J. Furthmüller, *Comput. Mater. Sci.* **6**, 15 (1996).
- [37] S. Grimme, J. Antony, S. Ehrlich, and H. Krieg, *J. Chem. Phys.* **132**, 154104 (2010).
- [38] S. Baroni, S. de Gironcoli, A. Dal Corso, and P. Giannozzi, *Rev. Mod. Phys.* **73**, 515 (2001).
- [39] J. Gao, Q. Wu, C. Persson, and Z. Wang, *Comput. Phys. Commun.* **261**, 107760 (2021).
- [40] G. Pizzi, V. Vitale, R. Arita, S. Blügel, F. Freimuth, G. Géranton, M. Gibertini, D. Gresch, C. Johnson, T. Koretsune, J. Ibañez-Azpiroz, H. Lee, J.-M. Lihm, D. Marchand, A. Marrazzo, Y. Mokrousov, J. I. Mustafa, Y. Nohara, Y. Nomura, L. Paulatto, S. Poncé, T. Ponweiser, J. Qiao, F. Thöle, S. S. Tsirkin, M. Wierzbowska, N. Marzari, D. Vanderbilt, I. Souza, A. A. Mostofi, and J. R. Yates, *J. Phys.: Condens. Matter* **32**, 165902 (2020).
- [41] Q. Wu, S. Zhang, H.-F. Song, M. Troyer, and A. A. Soluyanov, *Comput. Phys. Commun.* **224**, 405 (2018).
- [42] F. Tran and P. Blaha, *Phys. Rev. Lett.* **102**, 226401 (2009).
- [43] P. Blaha, K. Schwarz, G. K. Madsen, D. Kvasnicka, and J. Luitz, *WIEN2K, An Augmented Plane Wave+Local Orbitals Program for Calculating Crystal Properties* (Karlheinz Schwarz, Vienna University of Technology, Austria, 2001).
- [44] See Supplemental Material at <http://link.aps.org/supplemental/10.1103/PhysRevB.109.085102> for the detailed process of calculating the change of the filling anomaly, the optimized internal atomic position of  $\text{Pt}_3\text{P}_2\text{Te}_8$  under hydrostatic pressure of 0.5 GPa, 1.0 GPa and 1.5 GPa, and the schematic diagram of the (100) and (001) surfaces of  $\text{Pt}_3\text{P}_2\text{Te}_8$  we calculate.
- [45] Z. Wang, P. Zhang, G. Xu, L. K. Zeng, H. Miao, X. Xu, T. Qian, H. Weng, P. Richard, A. V. Fedorov, H. Ding, X. Dai, and Z. Fang, *Phys. Rev. B* **92**, 115119 (2015).
- [46] X. Ma, G. Wang, R. Liu, T. Yu, Y. Peng, P. Zheng, and Z. Yin, *Phys. Rev. B* **106**, 115114 (2022).
- [47] Z. Wang, Y. Sun, X.-Q. Chen, C. Franchini, G. Xu, H. Weng, X. Dai, and Z. Fang, *Phys. Rev. B* **85**, 195320 (2012).
- [48] C. Le, X. Wu, S. Qin, Y. Li, R. Thomale, F.-C. Zhang, and J. Hu, *Proc. Natl. Acad. Sci. USA* **115**, 8311 (2018).
- [49] M. Z. Hasan and C. L. Kane, *Rev. Mod. Phys.* **82**, 3045 (2010).
- [50] Y. Wu, N. H. Jo, L.-L. Wang, C. A. Schmidt, K. M. Neilson, B. Schruck, P. Swatek, A. Eaton, S. L. Bud'ko, P. C. Canfield, and A. Kaminski, *Phys. Rev. B* **99**, 161113(R) (2019).
- [51] C. Mondal, C. K. Barman, B. Pathak, and A. Alam, *Phys. Rev. B* **100**, 245151 (2019).
- [52] X. Zhao, F. Ma, and Z.-Y. Lu, *Phys. Rev. B* **104**, 235105 (2021).
- [53] M. Kargarian, Y.-M. Lu, and M. Randeria, *Phys. Rev. B* **97**, 165129 (2018).
- [54] M. Kargarian, M. Randeria, and Y.-M. Lu, *Proc. Natl. Acad. Sci. USA* **113**, 8648 (2016).
- [55] B. J. Wieder, Z. Wang, J. Cano, X. Dai, L. M. Schoop, B. Bradlyn, and B. A. Bernevig, *Nat. Commun.* **11**, 627 (2020).
- [56] M. Lin and T. L. Hughes, *Phys. Rev. B* **98**, 241103(R) (2018).
- [57] Sayed Ali Akbar Ghorashi, T. Li, and T. L. Hughes, *Phys. Rev. Lett.* **125**, 266804 (2020).
- [58] S. Nie, J. Chen, C. Yue, C. Le, D. Yuan, Z. Wang, W. Zhang, and H. Weng, *Sci. Bull.* **67**, 1958 (2022).
- [59] Y. Fang and J. Cano, *Phys. Rev. B* **104**, 245101 (2021).
- [60] B.-J. Yang, T. Morimoto, and A. Furusaki, *Phys. Rev. B* **92**, 165120 (2015).